Efficient Synthesis of Angular Selective Surfaces Based on Accurate Equivalent Circuit Analysis

Qin, Tao; Lin, Xian Qi; Yao, Yao ; Liu, Yong ; Liu, Hao ; Hao, Peng ; Mei, Peng

Published in:
I E E E Transactions on Microwave Theory and Techniques

DOI (link to publication from Publisher):
https://doi.org/10.1109/TMTT.2022.3232109

Publication date:
2022

Document Version
Accepted author manuscript, peer reviewed version

Efficient Synthesis of Angular Selective Surfaces Based on Accurate Equivalent Circuit Analysis

Tao Qin, *Student Member, IEEE,* Xian Qi Lin, *Senior Member, IEEE,* Yao Yao, Yong Liu, *Member, IEEE,* Hao Liu, *Member, IEEE,* Peng Hao, *Member, IEEE,* Peng Mei, *Member, IEEE*

***Abstract*—A new efficient synthesis method of angular selective surfaces (ASSs) based on the accurate equivalent circuit model is proposed. The angular dispersion of different components under oblique incidence is modeled by virtual lumped elements in the angular domain. The processes of obtaining the equivalent circuit for substrates, electrically small grids and patch arrays are presented in detail. The synthesized circuits are simple and accurate. Full-wave simulations are carried out to obtain the angular dispersion of different structures, and the calculated results are in good agreement with those of the equivalent circuit. A third-order ASS with bandpass response and a second-order ASS with a tunable bandwidth are given as design examples. The implemented second-order ASS shows the 0.33 to 0.52 tunable bandwidth in the angular domain. The transmission loss is better than 1.2 dB when the incidence angle is 65 to 77 degrees. The simulation results and calculated results are in good agreement with the measured results.**

***Index Terms*—Spatial angular filter, frequency selective surface, angular selective surface, equivalent circuit, meta-surface.**

I. Introduction

In the past decades, there has been considerable interest in frequency selective surface (FSS), for its versatility enables integration into all kinds of modern systems [1]–[5]. An invariant response over different incidence angles is always desired in most applications with a whole host of efforts to this end [6]–[10]. Detailed equivalent circuit analysis, well-developed filter synthesis and even machine learning technologies are already applied in related designs [11]–[15]. However, there has been little discussion on angular selective surfaces (ASSs), or spatial filters with an engineered response dependent on the incidence angle, and only a few papers have ever touched on this topic [16]–[24]. In 1976, Robert Mailloux proposed the first spatial filter and a synthesis method based on a cascaded scatter matrix and stepped impedance transmission line filter [16]. Consisting of several high permittivity substrates, this spatial filter has a synthesized Chebyshev response. In [17], a spatial filter is designed with cascaded metal grids and air spacers in between. It is used to suppress antenna side lobes, in which the spatial response of the grid array is analyzed using spatial harmonics. In [18], [19], a spatial filter comprised of substrate-supersaturates is used to enhance the antenna gain. A third-order spatial filter based on a third-order frequency filter is presented in [20] where the spatial filtering response is directly derived from the frequency domain. In [21], a multilayer dielectric angular filter is used to suppress grating lobes of a patch antenna array, reducing grating lobes by $15 \sim 30$ dB. Recently, a spatial angular filter based on a single-layer interconnected split-ring-resonators (SRRs) has been proposed in [22], greatly reduced the thickness of the filter compared with other designs [25].

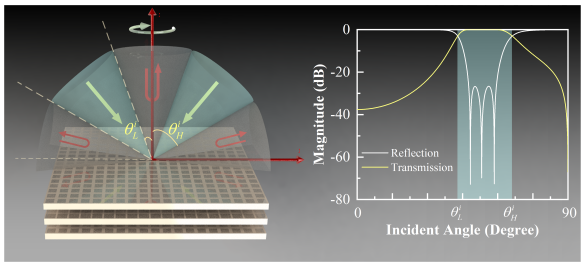

Fig. 1: The function of the proposed ASS. Different transmission characteristics can be obtained under different incidence angles, such as the bandpass response.

However, many of these syntheses or design methods presented in these papers still have some drawbacks. Specifically, the angular dispersion of the high dielectric substrates in [17] is considered to be negligible and excluded in the design process; the relationship between incidence angle and frequency domain in [20] limited the design freedom; the cascaded scattering matrix used in [17], [19], however, needs to be applied to the whole structure, but this would make the calculation cumbersome and difficult once the number of layers is increased. In a word, due to an absence of accurate circuit models comprised of transmission lines and equivalent lumped components related to the incidence angles, there is still a lack of a universal and direct spatial filter or ASS design method.

In this paper, the accurate equivalent circuits of several fundamental cells are examined to address the above problems. We present a new efficient synthesis method of angle selective

Manuscript received XX, 202X; revised XX, 202X; accepted XX, 202X. Date of publication XX, 202X; date of current version XX, 202X. This work was supported by in part by National Natural Science Foundation of China under Grant No. U1966201, in part by the Fundamental Research Funds for the Central Universities under Grant No. ZYGX2021J008, in part by Scientific Research Foundation for Yangtze Delta Region Institute of University of Electronic Science and Technology of China, Huzhou, under Grant Nos. U03210005, and in part by the China Scholarship Council under File No. 202206070058. (Corresponding authors: Xian Qi Lin and Peng Mei.)

Tao Qin, Xian Qi Lin, Yao Yao, Yong Liu, Hao Liu and Peng Hao are with the School of Electronic Engineering, University of Electronic Science and Technology of China, Chengdu 611731, China. and also with the Yangtze Delta Region Institute (Huzhou), University of Electronic Science and Technology of China, Huzhou 313001, P. R. China (e-mail: andyqint@gmail.com).

Peng Mei is with the Department of Electronic Systems, Aalborg University, 9220 Aalborg, Denmark (e-mail: mei@es.aau.dk).

surfaces based on the accurate equivalent circuit model, in which the angular dispersion of reactance and susceptance in the FSS structure is represented by virtual capacitors or inductors, or their combinations. Since these virtual capacitors and inductors are mathematical objects with no physical restrictions, the capacitance and inductance can be negative, which allows non-Foster behavior of the angular dispersion functions. Good consistencies are obtained between the theoretical calculation and simulation results in the whole process of analysis. A second-order ASS with a tunable bandwidth and a third-order ASS are demonstrated as design examples. Fig. 1 shows the function of this novel spatial ASS. Different transmission characteristics can be obtained under different incidence angles. On the basis of the existing literature, the major contributions of our work are summarized as follows:

a) Accurate equivalent circuit models of the basic FSS cells in the angular domain are presented. During the whole analysis process, the theoretical calculation is in good agreement with the simulation results, which not only guarantees solution accuracy, but also greatly reduces the computational load. The angular dispersion of the FSS can then be analyzed or synthesized using simple methods or pure numerical optimization that have already been developed in the circuits.

b) Electromagnetic properties of the proposed ASS are the function of the incidence angle, not the function of the electrical frequency. The ASS with such properties makes it a potential device in secure communications, radome design, energy harvesting, spatial multiplexing and anti-interference at a specific incidence angle. Based on this, a second-order ASS with tunable bandwidth in the angular domain is synthesized, fabricated and measured. And bandwidth tuning is realized directly by adjusting the distance between the substrates.

This paper is organized as follows: Part II defines the angular function in the angular domain and the necessary re-normalization process involved. In Part III, the equivalent circuits in the angular domain of substrates, electrically small grids and patches are summarized and verified numerically. The design procedure and the two examples are demonstrated in Part IV, and the experimental verification of the second-order ASS with tunable bandwidth is presented in Part V. Part VI discusses the responses of these designs in the frequency domain. Conclusions and further discussions are drawn in the final part.

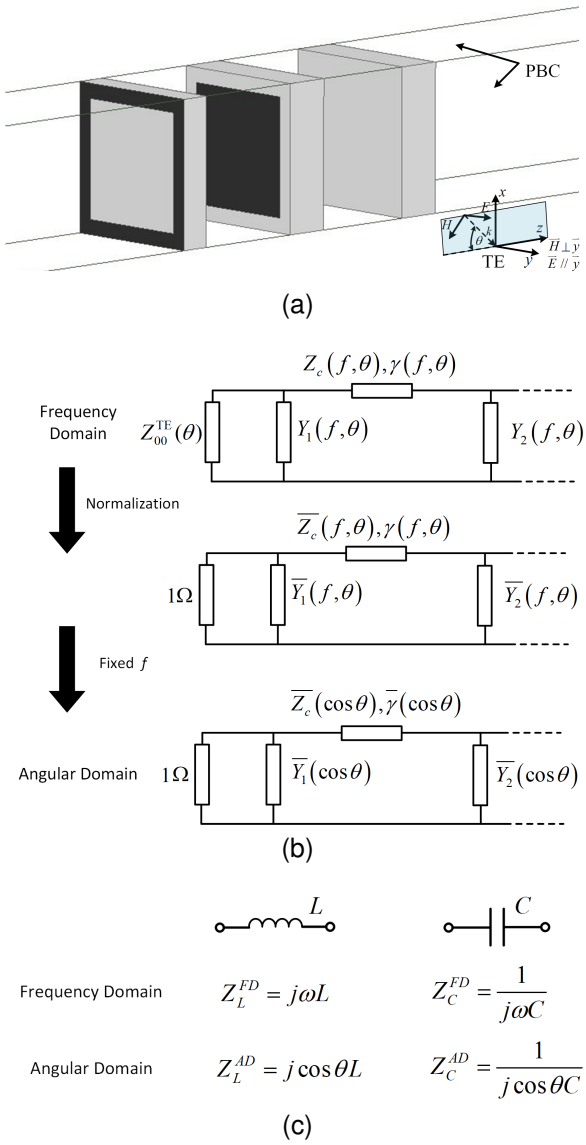

Fig. 2: The unit cell of an FSS and its equivalent circuits in the frequency domain and the angular domain (a) Unit cell of a general FSS under the TE incidence wave. (b) The equivalent circuits in the frequency domain and angular domain where the operating frequency is set and re-normalization is employed. (c) The impedance of basic components in the frequency domain and the angular domain, respectively.

II. ANGULAR DOMAIN AND NORMALIZATION

Fig. 2(a) shows the unit cells of a general FSS with the periodical structure in the XOY plane, which can be comprised of, for example, multiple substrates with etched metallic patterns on both sides and one or more air spacers between them. A plane wave propagates at an arbitrary angle θ with respect to the negative Z direction in the XOZ plane. In this setting, the electric field of the TE incidence wave will be polarized along the Y-axis, while the magnetic field of the TM incidence wave is polarized along the Y-axis. Some reasonable assumptions needed for further discussion are given below:

1) The unit cell of the FSS has a much smaller periodic D than the wavelength in free space at the frequency of interest, so only basic Floquet modes are presented in the reflected and transmitted waves, i.e., TE_{00} for TE incidence and TM_{00} for TM incidence. Higher modes are evanescent and decay exponentially from the cells [26]–[28].

2) There is no cross-polarization component between the reflected and transmitted waves, which is appropriate for planar passive FSS and electrically small periodic structures [1], [29].

3) The FSS is homogeneous in both X and Y directions and the geometric dimensions of the elements in the same layer are identical and not scaled so that no phase gradient occurs across the surface, ensuring that the reflection and transmission

angles remained at $-\theta$ and θ, respectively [2], [26], [27].

According to these assumptions, the frequency domain equivalent circuit shown in Fig. 2(b) can be used to study the multi-layer FSS's behavior under different incidence angles. In this circuit, the shunt components represent the metallic patterns and the transmission lines represent substrates or air-spacers. The port impedance of this two-port network is the Floquet modal impedance corresponding to the incidence wave, which is analyzed in this paper. The TE_z modal fields, for example, have no electric field component along z by definition. The TE_z modal field components can be generated from an electric vector potential $\overrightarrow{F}$ that has only a z-component. It can be expressed as [26]:

$$\overrightarrow{F} = \hat{z} A \exp(-jk_{xmn}x - jk_{ymn}y - jk_{zmn}z) \tag{1}$$

where A is a constant related to the amplitude, which is not discussed here. k_{xmn} and k_{ymn} are the mode numbers for the TE_z Floquet mode. The symbol (m, n) is used to represent either the TE_z or the TM_z Floquet modes.

As mentioned in the former assumptions, only the basic Floquet modes are presented here. For $m = n = 0$, k_{x00}, k_{y00} are equal to the phase constants related to the intended radiation direction, which are given by:

$$k_{x00} = k_0 \sin\theta \cos\phi \tag{2a}$$

$$k_{y00} = k_0 \sin\theta \sin\phi \tag{2b}$$

where k_0 is the wave number in free space, and (θ, ϕ) is the intended radiation direction in the spherical coordinate system.

Then the wave number along z is obtained as:

$$k_{z00} = \sqrt{k_0^2 - k_{x00}^2 - k_{y00}^2} = k_0 \cos\theta \tag{3}$$

Therefore the modal impedance for TE_{00} can be expressed as:

$$Z_{00}^{\mathrm{TE}} = \frac{\left|\overrightarrow{E}\right|}{\left|\overrightarrow{H}\right|} = \frac{|j\omega\mu| \left|-\nabla \times \overrightarrow{F}\right|}{\left|\nabla \times (-\nabla \times \overrightarrow{F})\right|} = \frac{\eta_0}{\cos\theta} \tag{4}$$

where ω is the angular frequency, μ is the permeability, and η_0 is the free-space impedance, which is equal to 120π ohms.

The modal impedance of TM_{00} obtained by using magnetic vector potential and similar procedures is given by:

$$Z_{00}^{\mathrm{TM}} = \eta_0 \cos\theta \tag{5}$$

Eq. (4) and Eq. (5) indicate that when analyzing equivalent circuits of FSSs in the frequency domain, the port impedance is only a function of θ and independent of f. But for the shunt components introduced by metal patterns as shown in Fig. 2(b), these parameters are generally the functions of both incidence angle and operating frequency. In most of the existing FSS analyses and designs, the incidence angle is usually fixed at around $0°$, that is, the incidence wave is perpendicular to the selective surface. However, in order to establish an effective synthesis method in the angular domain, a much more accurate model is required.

Given that the re-normalization of the impedance does not affect the scattering parameters of transmission lines [30], [31], a normalization is adopted firstly. Then, the port impedance

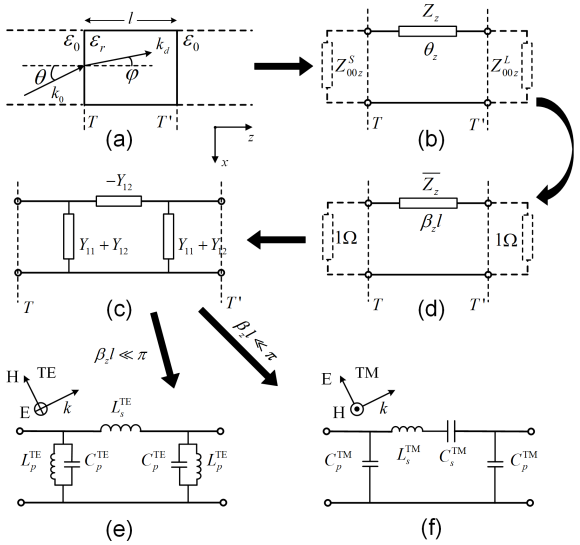

Fig. 3: A substrate under oblique incidence and its angular domain equivalent circuit. Under the TE incidence wave, it has a series inductor, two parallel capacitors and two parallel inductors. As for the TM incidence wave, it has a series capacitor, a series inductor and two parallel capacitors.

becomes 1 ohm, but the values of these shunt components are still functions of both θ and f. Once the operating frequency is fixed, values of all these components are functions of θ. And the equivalent circuit in the angular domain is finally obtained.

For a better understanding of the relationship between the angular domain and the frequency domain, Fig. 2(c) shows several basic elements and their equivalent impedance in these two domains. In the frequency domain, the normalized port impedance is usually 1 ohm in the equivalent circuits of filter synthesis. The equivalent impedance of an inductor with inductance L is $j\omega L$, which is only related to the operating frequency f (or $2\pi f$) and the value of L. In the angular domain, after the previous normalization, the port impedance is 1, and the equivalent impedance of the same inductor becomes $j\cos\theta L$, which is related to the value of incidence angle θ (or $\cos\theta$) and L. But, when focusing on the response function of these elements or their combinations, classical theories such as filter theory and even-odd mode analysis can be reasonably applied in both frequency domain and angular domain. Simply speaking, normalization and fixed frequency are the transformations of these two domains. The re-normalization method discussed here will be adopted in the following analyses, and the operating frequency of all the proposed designs will be fixed at 10 GHz. Notably, for propagating plane waves, the angular function $\cos\theta$ is confined to $[0, 1]$, corresponding to θ in $[0°, 90°]$.

III. Equivalent Circuits of the Basic FSS Cells in the Angular Domain

A. Free space filled with dielectric

Some basic FSS cells, i.e., free spaces filled with dielectrics, metallic patches and grids on the substrate, are discussed in this part. The detailed process of obtaining equivalent circuits

in the angular domain is given and the numerical validation is carried out.

Consider the substrate with relative permittivity ε_r under the incidence wave as shown in Fig. 3(a), θ is the incidence angle in the free space and φ is the refracted angle in the substrate, which can be defined from Snell's law [32]:

$$\cos\varphi = \sqrt{\frac{\varepsilon_r - \sin^2\theta}{\varepsilon_r}} = \sqrt{\frac{\varepsilon_r - 1 + \cos^2\theta}{\varepsilon_r}} \tag{6}$$

The wave number in the substrate k_d is given by:

$$k_d = 2\pi f\sqrt{\varepsilon_r\varepsilon_0\mu_0} = k_0\sqrt{\varepsilon_r} \tag{7}$$

Since the homogeneous media and characteristics are discussed along the direction perpendicular to the interface, $+z$ direction here, the substrate between the two reference planes TT' is equivalent to a section of the transmission line as shown in Fig. 3(b). The characteristic impedance of this transmission line is equal to the modal impedance in the substrate, which can be expressed as:

$$Z_{dz}^{\mathrm{TE}} = \frac{\eta_d}{\cos\varphi} = \frac{\eta_0}{\sqrt{\varepsilon_r}\cos\varphi} \tag{8a}$$

$$Z_{dz}^{\mathrm{TM}} = \eta_d\cos\varphi = \frac{\eta_0\cos\varphi}{\sqrt{\varepsilon_r}} \tag{8b}$$

The electric length of this transmission line is given by:

$$\theta_z = \beta_z l = (k_d\cos\varphi)l = \beta_0 l\sqrt{\varepsilon_r}\cos\varphi \tag{9}$$

where Eq. (7) and the propagation constant in free space: $\beta_0 = k_0$ are substituted to simplify.

Then, as shown in Fig. 3(d), the normalized ABCD matrix is written as:

$$\begin{bmatrix} A & B \\ C & D \end{bmatrix} = \begin{bmatrix} \cos\theta_z & j\overline{Z_{dz}}\sin\theta_z \\ \frac{j}{\overline{Z_{dz}}}\sin\theta_z & \cos\theta_z \end{bmatrix} \tag{10}$$

where:

$$\overline{Z_{dz}^{\mathrm{TE}}} = \frac{Z_{dz}^{\mathrm{TE}}}{Z_{00}^{\mathrm{TE}}} = \frac{\cos\theta}{\sqrt{\varepsilon_r}\cos\varphi} \tag{11a}$$

$$\overline{Z_{dz}^{\mathrm{TM}}} = \frac{Z_{dz}^{\mathrm{TM}}}{Z_{00}^{\mathrm{TM}}} = \frac{\cos\varphi}{\sqrt{\varepsilon_r}\cos\theta} \tag{11b}$$

For further synthesis, considering a typical symmetric π-shape equivalent circuit shown in Fig. 3(c), its ABCD matrix is given by:

$$\begin{bmatrix} A & B \\ C & D \end{bmatrix} = \begin{bmatrix} -\frac{Y_{11}}{Y_{12}} & -\frac{1}{Y_{12}} \\ -\frac{Y_{11}^2}{Y_{12}} + Y_{12} & -\frac{Y_{11}}{Y_{12}} \end{bmatrix} \tag{12}$$

The equivalence of these two circuits as shown in Fig. 3, that is, Eq. (12) is equal to Eq. (10), can be achieved under the following conditions:

$$\frac{-1}{Y_{12}} = j\overline{Z_{dz}}\sin\theta_z \tag{13a}$$

$$Y_{12} + Y_{11} = \frac{\cos\theta_z - 1}{j\overline{Z_{dz}}\sin\theta_z} \tag{13b}$$

Importantly, when $\beta_0 l\sqrt{\varepsilon_r}\cos\varphi \le \pi/18$, which means an infinitesimally thin slice of the substrate, Eq. (13) can be simplified by substituting Eqs. (6), (9), (11) and the following equivalent infinitesimal:

$$\sin x \sim_0 x \tag{14a}$$

$$\frac{\cos^2 x - 1}{\sin x} \sim_0 -\frac{x}{2} \tag{14b}$$

Then, the simplified results are presented here:
For TE incidence wave:

$$\frac{-1}{Y_{12}} = j\cos\theta\beta_0 l \tag{15a}$$

$$Y_{12} + Y_{11} = j\cos\theta\frac{\beta_0 l}{2} + \frac{1}{j\cos\theta\frac{-2}{(\varepsilon_r-1)\beta_0 l}} \tag{15b}$$

For TM incidence wave:

$$\frac{-1}{Y_{12}} = j\cos\theta\frac{\beta_0 l}{\varepsilon_r} + \frac{1}{j\cos\theta\frac{-\varepsilon_r}{(\varepsilon_r-1)\beta_0 l}} \tag{16a}$$

$$Y_{12} + Y_{11} = j\cos\theta\frac{\varepsilon_r\beta_0 l}{2} \tag{16b}$$

According to Eq. (15), in the angular domain where values of the equivalent elements are the functions of $\cos(\theta)$, the equivalent circuit of a substrate with relative permittivity ε_r under the TE incidence wave, as shown in Fig. 3, has a series inductor, two parallel capacitors and two parallel inductors, and the capacitance and inductance are given as follows:

$$L_{\mathrm{s}}^{\mathrm{TE}} = \beta_0 l \tag{17a}$$

$$L_{\mathrm{p}}^{\mathrm{TE}} = -\frac{2}{(\varepsilon_r - 1)\beta_0 l} \tag{17b}$$

$$C_{\mathrm{p}}^{\mathrm{TE}} = \frac{\beta_0 l}{2} \tag{17c}$$

According to Eq. (16), the equivalent circuit of a substrate with relative permittivity ε_r under the TM incidence wave shown in Fig. 3, has a series inductor, a series capacitor and two parallel capacitors, and its capacitance and inductance are as follows:

$$L_{\mathrm{s}}^{\mathrm{TM}} = \frac{\beta 1_0 l}{\varepsilon_r} \tag{18a}$$

$$C_{\mathrm{s}}^{\mathrm{TM}} = -\frac{\varepsilon_r}{(\varepsilon_r - 1)\beta_0 l} \tag{18b}$$

$$C_{\mathrm{p}}^{\mathrm{TM}} = \frac{\varepsilon_r\beta_0 l}{2} \tag{18c}$$

B. Metallic patches and grid

Fig. 4 shows the electrically small patch array and its complementary structure grid. As simple and basic cells in FSS designs, plenty of works have focused on the analysis of their equivalent circuits in the frequency domain [29], [33]–[40]. When the periodic D is electrically small and $w \ll D$, the shunt impedance of the gird and patch can be given as:
For TE incidence wave [39]:

$$Z_{\mathrm{grid}}^{\mathrm{TE}} = j\frac{\eta_{\mathrm{eff}}}{2}\alpha \tag{19a}$$

$$Z_{\mathrm{patch}}^{\mathrm{TE}} = -j\frac{\eta_{\mathrm{eff}}}{2\alpha(1 - \frac{\beta_0^2\sin^2\theta}{2\beta_{\mathrm{eff}}^2})} \tag{19b}$$

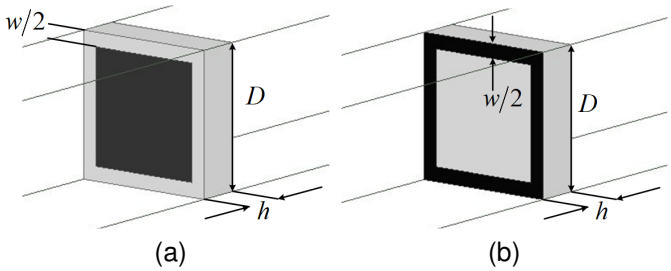

Fig. 4: The geometry of the metallic grid and metallic patch on substrates. (a) The array of patches in a homogeneous host medium. (b) A mesh of ideally conducting strips in a homogeneous host medium. Metal parts are colored black.

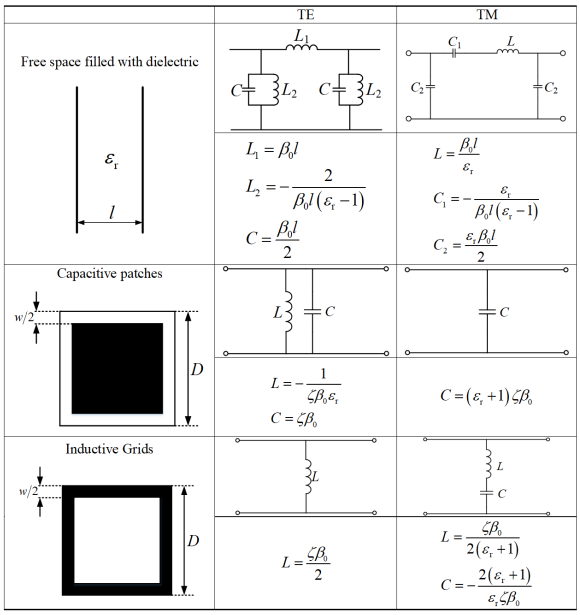

Fig. 5: Summarized equivalent circuits in the angular domain of the basic FSS cells under different polarization.

For TM incidence wave [39]:

$$Z_{\text{grid}}^{\text{TM}} = j\frac{\eta_{\text{eff}}}{2}\alpha(1-\frac{\beta_0^2\sin^2\theta}{2\beta_{\text{eff}}^2}) \tag{20a}$$

$$Z_{\text{patch}}^{\text{TM}} = -j\frac{\eta_{\text{eff}}}{2\alpha} \tag{20b}$$

Here, $\eta_{\text{eff}} = \eta_0/\sqrt{\varepsilon_{\text{eff}}}$ and $\beta_{\text{eff}} = \beta_0\sqrt{\varepsilon_{\text{eff}}}$ refer to the wave impedance and wave number in the effective host medium where the patch array or grid is located, respectively. A good approximation for the effective permittivity of the host medium ε_{eff} is given by $\varepsilon_{\text{eff}} = (\varepsilon_{\text{r}}+1)/2$ [41]. α is a geometry parameter defined as [42]:

$$\alpha = \frac{\beta_{\text{eff}}D}{\pi}[\ln(\frac{1}{\sin\frac{\pi w}{2D}}) + \sum_{i=1}^{\infty}\frac{(2i-1)\Gamma(2i+1)}{2^{2i-1}}\left(\frac{\beta_{\text{eff}}D}{2\pi}\right)^{2i}] \tag{21}$$

where Γ is the Riemann zeta-function and the terms with Γ can be negligible when $|\beta_{\text{eff}}D| \ll 2\pi$ [42].

Eq. (19) and Eq. (20) can be re-normalized in the same way as mentioned previously, and the normalized shunt impedance after mathematical processing are:

For TE incidence wave:

$$\overline{Z}_{\text{grid}}^{\text{TE}} = j\cos\theta\frac{\beta_0\zeta}{2} \tag{22a}$$

$$\overline{Z}_{\text{patch}}^{\text{TE}} = \frac{1}{j\cos\theta\beta_0\zeta + \frac{1}{j\cos\theta\frac{-1}{\varepsilon_{\text{r}}\beta_0\zeta}}} \tag{22b}$$

where:

$$\zeta = \frac{D}{\pi}\ln(\frac{1}{\sin\frac{\pi\omega}{2D}}) \tag{23}$$

For TM incidence wave:

$$\overline{Z}_{\text{grid}}^{\text{TM}} = j\cos\theta\frac{\beta_0\zeta}{2(\varepsilon_{\text{r}}+1)} + \frac{1}{j\cos\theta\frac{-2(\varepsilon_{\text{r}}+1)}{\varepsilon_{\text{r}}\beta_0\zeta}} \tag{24a}$$

$$\overline{Z}_{\text{patch}}^{\text{TM}} = \frac{1}{j\cos\theta(\varepsilon_{\text{r}}+1)\beta_0\zeta} \tag{24b}$$

It can be seen in Eq. (22) that under the TE incidence wave, the grid shunt impedance is that of a positive inductor while the patch array has a conductance of a parallel capacitor and a parallel negative inductor as shown in Fig. 5. The values of the equivalent inductance and capacitance are:

$$L_{\text{grid}}^{\text{TE}} = \frac{\beta_0\zeta}{2} \tag{25a}$$

$$L_{\text{patch}}^{\text{TE}} = -\frac{1}{\varepsilon_{\text{r}}\beta_0\zeta} \tag{25b}$$

$$C_{\text{patch}}^{\text{TE}} = \beta_0\zeta \tag{25c}$$

It is apparent from Eq. (24) that under the TM incidence wave, the grid shunt impedance is that of a series inductor and a series capacitor with a negative value, while the patch array has a conductance of a positive capacitor as shown in Fig. 5, and the capacitance and inductance are as follows:

$$L_{\text{grid}}^{\text{TM}} = \frac{\beta_0\zeta}{2(\varepsilon_{\text{r}}+1)} \tag{26a}$$

$$C_{\text{grid}}^{\text{TE}} = -\frac{2(\varepsilon_{\text{r}}+1)}{\varepsilon_{\text{r}}\beta_0\zeta} \tag{26b}$$

$$C_{\text{patch}}^{\text{TE}} = (\varepsilon_{\text{r}}+1)\beta_0\zeta \tag{26c}$$

C. Numerical validation

The aforementioned conclusions are summarized and listed in Fig. 5. Numerical simulation is performed to validate the obtained equivalent circuits.

The S-parameters of the substrates, the grid and the patch array are illustrated in Fig. 6. The relative permittivity of the lossless substrates used is 2 and the dimensions of the metallic patterns are $D = 7mm, w = 1mm, h = 1mm$, which means $\zeta = 0.123$ for metallic patches and grids. The calculated elemental values under different conditions are also given. To obtain the calculated results, circuit analysis and matrix operations of microwave networks are adopted here. For example, for the metallic patch under TM polarization, the cascaded ABCD matrix of the metallic patch and substrate can be written as:

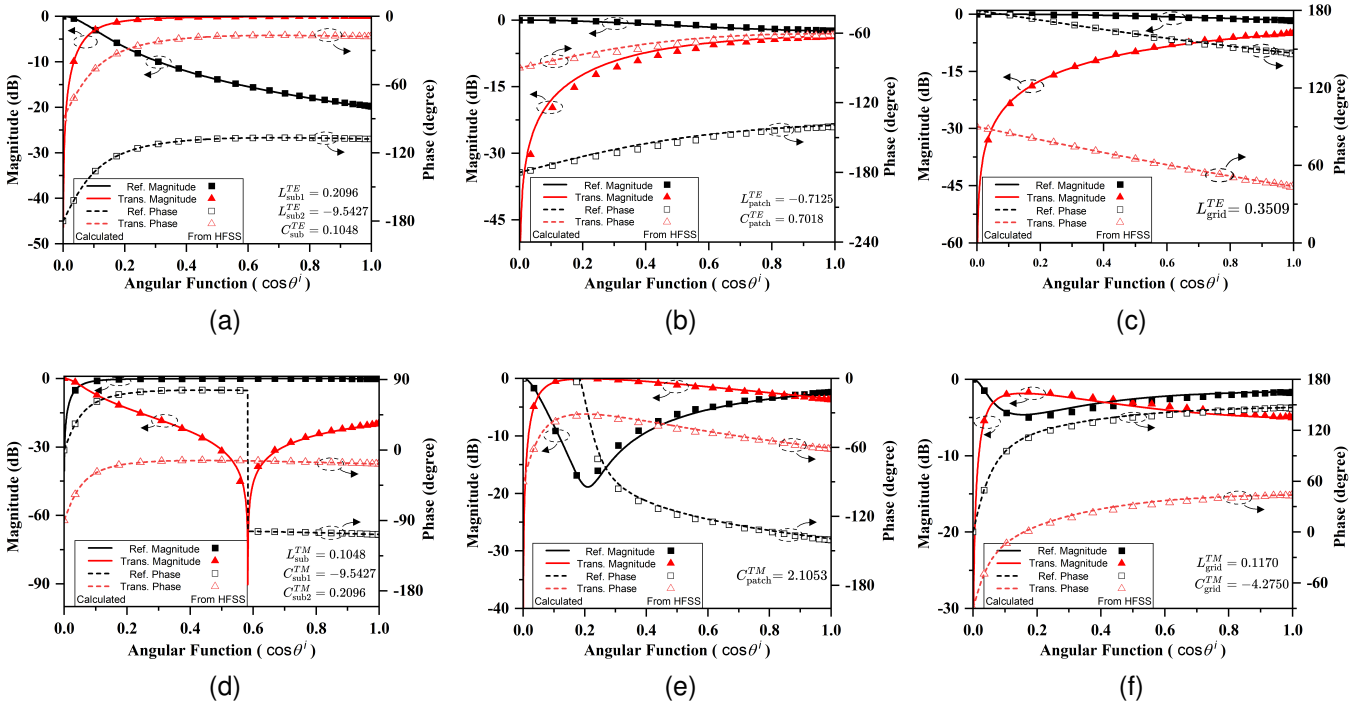

Fig. 6: The numerical validation of the equivalent circuits shown in Fig. 5. The simulation results obtained by the full-wave simulation are represented by the solid lines without markers, while the calculated results obtained by the mathematical calculation are represented by pure markers. (a) substrate under TE incidence (b) patch under TE incidence (c) grid under TE incidence (d) substrate under TM incidence (e) patch under TM incidence (f) grid under TM incidence.

$$\begin{aligned}\left[A^{\mathrm{TM}}_{\mathrm{total}}\right] &= \left[A^{\mathrm{TM}}_{\mathrm{patch}}\right]\left[A^{\mathrm{TM}}_{\mathrm{sub}}\right] \\ &= \left[A^{\mathrm{TM}}_{\mathrm{patch_C}}\right]\left[A^{\mathrm{TM}}_{\mathrm{sub_{C2}}}\right]\left[A^{\mathrm{TM}}_{\mathrm{sub_{C1}}}\right]\left[A^{\mathrm{TM}}_{\mathrm{sub_L}}\right]\left[A^{\mathrm{TM}}_{\mathrm{sub_{C2}}}\right] \\ &= \begin{bmatrix} 0.978 - 0.022\tau^2 & j(\frac{0.105}{\tau} + 0.105\tau) \\ j(2.473\tau - 0.051\tau^3) & 0.757 - 0.243\tau^2 \end{bmatrix}\end{aligned} \tag{27}$$

where τ is the angular function ($\cos\theta$). $\left[A^{\mathrm{TM}}_{\mathrm{patch_C}}\right]$, $\left[A^{\mathrm{TM}}_{\mathrm{sub_{C2}}}\right]$, $\left[A^{\mathrm{TM}}_{\mathrm{sub_{C1}}}\right]$ and $\left[A^{\mathrm{TM}}_{\mathrm{sub_L}}\right]$ are the ABCD matrix of corresponding equivalent elements shown in Fig. 5. Using the conversion formulas between ABCD matrix and [S] matrix [31], the calculated S-parameters can be obtained:

$$\begin{aligned} S_{11} &= \frac{-2.06 + j0.34\tau + 46.59\tau^2 + j4.77\tau^3 - \tau^4}{-2.06 + j34.13\tau - 50.71\tau - j4.77\tau^2 + \tau^3} \\ S_{21} &= \frac{j39.33\tau}{-2.06 + j34.13\tau - 50.71\tau - j4.77\tau^2 + \tau^3} \end{aligned} \tag{28}$$

In Fig. 5, the simulation results obtained by the full-wave simulation using HFSS (High Frequency Structure Simulator) are represented by the solid lines without markers, while the calculated results are represented by pure markers. Except for tiny deviations, all these simulation results are in good agreement with the calculated ones.

IV. Designing Examples and Procedures

A. Equivalent Inverter under TM Incidence Wave

As shown in Fig. 5, the equivalent circuit of a substrate with relative permittivity ε_r under the TM incidence wave has a series capacitor with the negative value, a series inductor and two parallel capacitors; the equivalent circuit of a patch array under the TM incidence wave has a parallel capacitor with a positive value. Therefore, an equivalent J-inverter under TM polarization, as shown in Fig. 7(a), can be realized by a structure that is obtained by etching two same metallic patches on both sides of a substrate with high permittivity. Fig. 7(a) depicts the simplified equivalent circuit of the inverter in which the series inductance is negligible due to the high permittivity of the substrate. The numerical validation of the inverter is demonstrated in Fig. 7(b), and the physical dimensions are as follows: $D = 3mm, w = 0.29mm, h = 1mm$, which means the value of the equivalent inverter is $J = 1/5.29\cos\theta$ and the reflection zero occurs when $\cos\theta = 0.189$. As can be seen in Fig. 7(b), the simulated results are in good agreement with the calculated results. Additionally, Fig. 7(c) shows simulation results of the same structure under TE incidence wave. Since its equivalent circuits are quite different from the one under the TM incidence wave, there is no reflection zero in the angular domain although good consistency between the simulation and calculation is maintained. The following sections only discuss the equivalent circuits and designs under TM polarization. The equivalent circuit under TE polarization can be obtained by referring to Fig. 5 and the relevant analysis method is basically

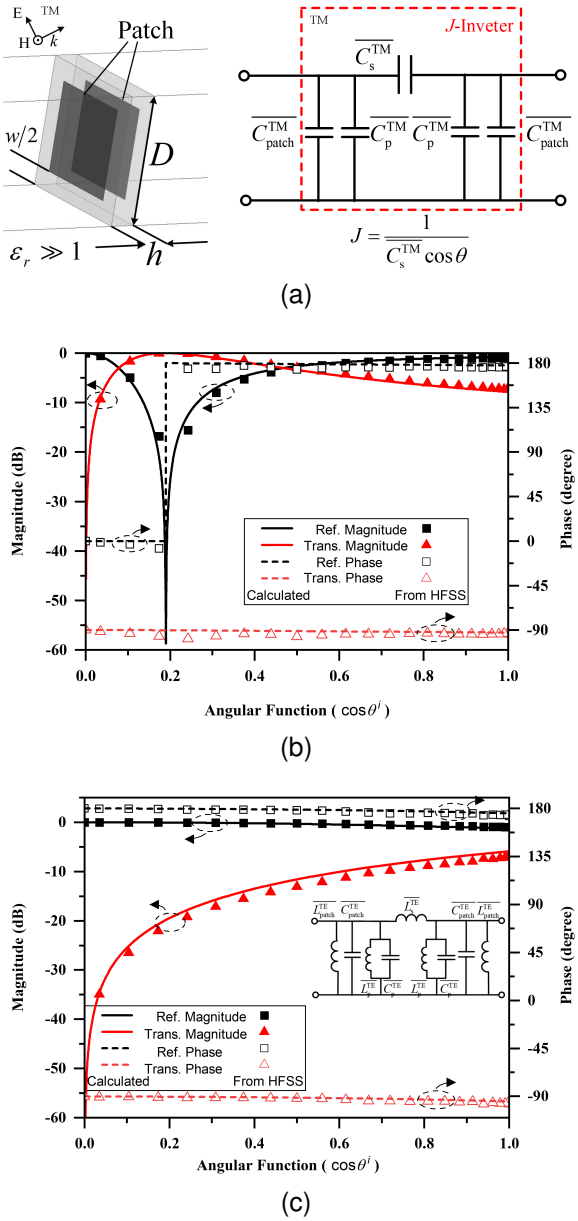

Fig. 7: The equivalent J-inverter in the angular domain (a) Geometry and its equivalent circuits (b) The numerical validation under TM mode. The reflection zero occurs when $\cos\theta = 0.189$ (c) Numerical validation under TE mode.

consistent with TM polarization.

Note that the equivalent inverter shown in Fig. 7(a) is sensible and realizable only when $-\overline{C_{\mathrm{s}}^{\mathrm{TM}}} \geq \overline{C_{\mathrm{p}}^{\mathrm{TM}}}$, which meets the following condition:

$$\beta_0 l \leq \frac{2}{\varepsilon_r - 1} \tag{29}$$

Besides, once the thickness and permittivity of the substrate are selected, the values of $\overline{C_{\mathrm{s}}^{\mathrm{TM}}}$ and $\overline{C_{\mathrm{p}}^{\mathrm{TM}}}$ are fixed, and the corresponding achievable inverter is determined.

B. Examples One: A third-order ASS

The structure and the equivalent circuits of the proposed ASSs are presented in Fig. 8. As the permittivity of air is close to 1, the series capacitor in the equivalent circuit of the air spacer is reasonably ignored. Some of the equivalent parallel capacitors of the patch, the substrate and the air spacer constitute the parallel capacitor of the J-inverter. The

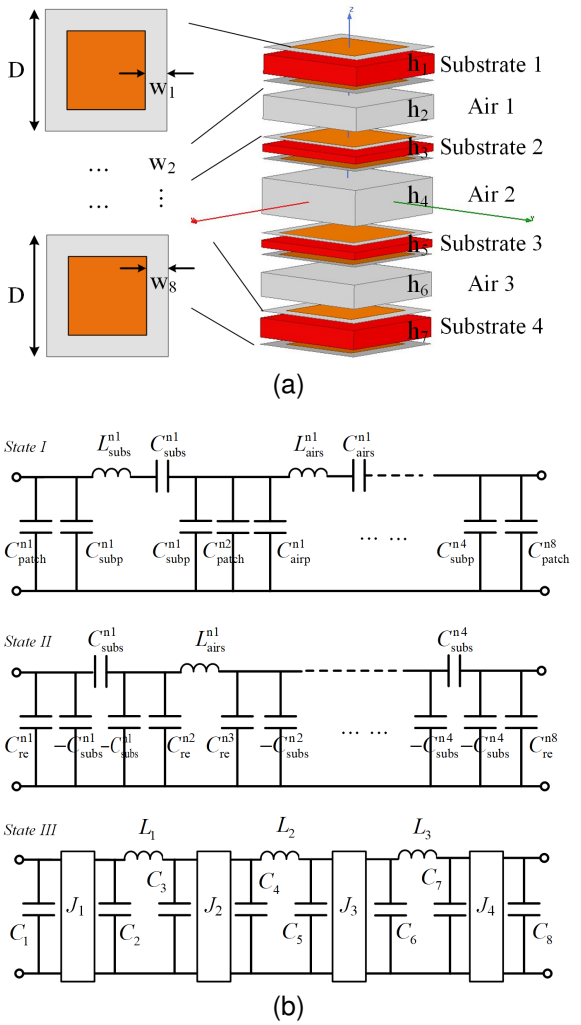

Fig. 8: The proposed ASS in the angular domain (a) The layout (b) Synthesis of its equivalent circuits. Compared with State I, the series inductance of the substrate and series capacitance of the air space is neglected reasonably in State II and State III. The equivalent J-inverter in the angular domain is also employed here.

TABLE I: Synthesized Values in the Equivalent Elements of a Third-Order Spatial ASS design

$C_1 = C_8$	$C_2 = C_7$	$C_3 = C_6$	$C_4 = C_5$	$L_1 = L_3$	L_2
-2.669	-2.040	0.563	0.563	1.258	1.258
$J_1 = J_2 = J_3 = J_4 = 1/5.289\cos\theta$					

TABLE II: Physical Dimensions of the Third-Order Spatial ASS

$w_1 = w_8$	$w_2 = w_7$	$w_3 = w_6$	$w_4 = w_5$	$h_2 = h_6$	h_4
1 mm	0.3 mm	1 mm	0.3 mm	6 mm	6 mm
$\varepsilon_1 = \varepsilon_2 = \varepsilon_3 = \varepsilon_4 = 10.2$			$h_1 = h_3 = h_5 = h_7 = 1mm$		

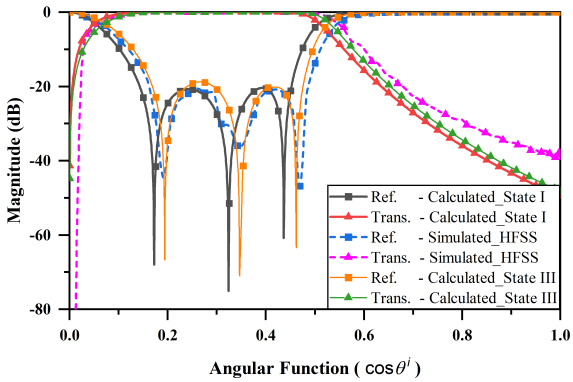

Fig. 9: Numerical validation of the proposed third-order ASS. In State III, the parallel inductance of the air spacer and the series inductance of the substrate are ignored compared with State I.

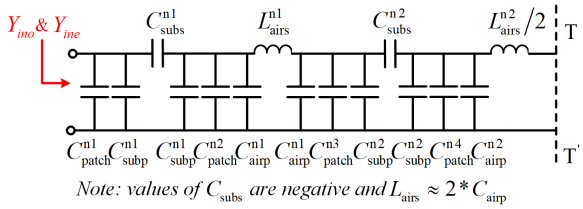

Fig. 10: Equivalent circuit of the proposed second-order passband ASS by using the even-odd-mode analysis where TT' is the symmetry plane.

TABLE III: Synthesized Values of the Equivalent Elements during the Second-Order ASS design

$w_1 = w_8$	$w_2 = w_7$	$w_3 = w_6$	$w_4 = w_5$
0.3 mm	0.3 mm	0.3 mm	0.3 mm
$\varepsilon_1 = \varepsilon_2 = \varepsilon_3 = \varepsilon_4 = 10.2$		$h_1 = h_3 = h_5 = h_7 = 1.2mm$	

relationship among these equivalent elements is given as follows:

$$\begin{aligned}
&C_1 = C^{\mathrm{n1}}_{\mathrm{re}} = C^{\mathrm{n1}}_{\mathrm{patch}} + C^{\mathrm{n1}}_{\mathrm{subp}} + C^{\mathrm{n1}}_{\mathrm{subs}} \\
&C_2 = C^{\mathrm{n2}}_{\mathrm{re}} = C^{\mathrm{n2}}_{\mathrm{patch}} + C^{\mathrm{n1}}_{\mathrm{subp}} + C^{\mathrm{n1}}_{\mathrm{subs}} + C^{\mathrm{n1}}_{\mathrm{airp}} \\
&\ldots \\
&C_7 = C^{\mathrm{n7}}_{\mathrm{re}} = C^{\mathrm{n7}}_{\mathrm{patch}} + C^{\mathrm{n4}}_{\mathrm{subp}} + C^{\mathrm{n4}}_{\mathrm{subs}} + C^{\mathrm{n3}}_{\mathrm{airp}} \\
&C_8 = C^{\mathrm{n8}}_{\mathrm{re}} = C^{\mathrm{n8}}_{\mathrm{patch}} + C^{\mathrm{n4}}_{\mathrm{subp}} + C^{4}_{\mathrm{subs}} \\
&J_i = \left| \frac{1}{C^{\mathrm{ni}}_{\mathrm{stubs}} \cos\theta} \right|, (i = 1, 2, 3, 4) \\
&L_j = L^{\mathrm{nj}}_{airs}, (j = 1, 2, 3)
\end{aligned} \tag{30}$$

Substitute the equations from Fig. 5 and the dimensions shown in Fig. 8(a) into Eq. (30), the simplified values in the equivalent circuit are:

$$\begin{aligned}
&C_1 = (\varepsilon_1 + 1)\zeta_{(D,w_1)} + \frac{\varepsilon_1 \beta_0 h_1}{2} - \frac{\varepsilon_1}{\beta_0 h_1 (\varepsilon_1 - 1)} \\
&C_2 = (\varepsilon_1 + 1)\zeta_{(D,w_2)} + \frac{\varepsilon_1 \beta_0 h_1}{2} - \frac{\varepsilon_1}{\beta_0 h_1 (\varepsilon_1 - 1)} + \frac{\beta_0 h_2}{2} \\
&\ldots \\
&C_7 = (\varepsilon_4 + 1)\zeta_{(D,w_7)} + \frac{\varepsilon_4 \beta_0 h_7}{2} - \frac{\varepsilon_4}{\beta_0 h_7 (\varepsilon_4 - 1)} + \frac{\beta_0 h_6}{2} \\
&C_8 = (\varepsilon_4 + 1)\zeta_{(D,w_8)} + \frac{\varepsilon_4 \beta_0 h_7}{2} - \frac{\varepsilon_4}{\beta_0 h_7 (\varepsilon_4 - 1)} \\
&J_i = \left| \frac{(\varepsilon_i - 1)\beta_0 h_{2i-1}}{\varepsilon_i \cos\theta} \right|, (i = 1, 2, 3, 4) \\
&L_j = \beta_0 h_{2j}, (j = 1, 2, 3)
\end{aligned} \tag{31}$$

where ε_1, ε_2, ε_3, ε_4 are the permittivity of the four substrates, respectively. $\zeta_{(D,w_{k=1,2,\ldots,8})}$ are the geometry parameters that can be determined by Eq. (21) and Eq. (23).

After obtaining the simplified equivalent circuits here, the values of other elements can be synthesized using the classical methods of filter design [30], [43], [44]. Note that once the substrates are selected, the relevant value of the equivalent J-inverter is determined. Therefore the actual dimensions and the permittivity of the substrates should be taken into account in the first place.

The synthesized element values and the corresponding physical dimensions of the third-order spatial ASS are listed in Table. I and Table. II, respectively. The numerical validation of this design is demonstrated in Fig. 9 with only small deviations between the calculation and simulation. The passband of this ASS is $[0.08, 0.48]$ in the angular domain, corresponding to the incidence angle of $[61°, 84°]$.

C. Examples Two: A second-order passband ASS with tunable bandwidth

In the design process mentioned above, the equivalent J-inverter is adopted, and those equivalent elements with negative values are absorbed into the inverter. However, since the accurate equivalent circuits of the model have been obtained, all these physical dimensions can be determined directly by numerical optimization. The symmetrical structure shown in Fig. 10 is adopted here, and the even-odd-mode analysis is used to determine the resonant angular function.

As for the odd-mode resonance, an equivalent electric wall is inserted at the symmetry plane TT' of the equivalent circuit shown in Fig. 10, and the one-port input admittance is derived as:

$$Y_{ino} = j(\tau C_1 + (\frac{1}{C^{\mathrm{n1}}_{subs}\tau} + \frac{1}{\tau C_2 - \frac{1}{L^{\mathrm{n1}}_{airs}\tau - Y_A}})^{-1}) \tag{32}$$

where τ is the angular function $\cos\theta$ and

$$\begin{aligned}
&\tfrac{1}{Y_A} = \\
&\tau \left(C^{\mathrm{n2}}_{subs} + C_3 - \frac{(C^{\mathrm{n2}}_{subs})^2 C^{\mathrm{n2}}_{airp} \tau^2}{-1 + C^{\mathrm{n2}}_{subs} C^{\mathrm{n2}}_{airp} \tau^2 + C_4 C^{\mathrm{n2}}_{airp} \tau^2} \right)
\end{aligned} \tag{33}$$

$$C_1 = C^{\mathrm{n1}}_{patch} + C^{\mathrm{n1}}_{subp} \tag{34}$$

$$C_2 = C^{\mathrm{n2}}_{patch} + C^{\mathrm{n1}}_{subp} + C^{\mathrm{n1}}_{airp} \tag{35}$$

$$C_3 = C^{\mathrm{n3}}_{patch} + C^{\mathrm{n2}}_{airp} + C^{\mathrm{n2}}_{subp} \tag{36}$$

$$C_4 = C^{\mathrm{n4}}_{patch} + C^{\mathrm{n2}}_{subp} + C^{\mathrm{n2}}_{airp} \tag{37}$$

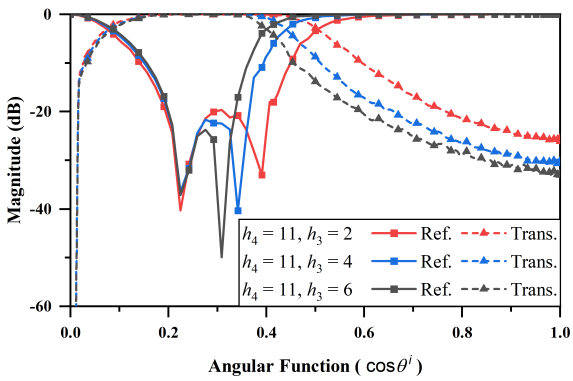

(a)

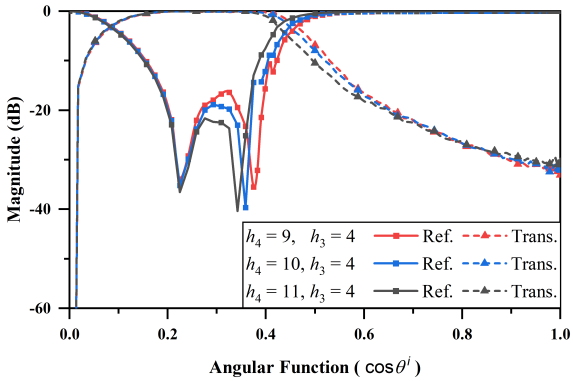

(b)

Fig. 11: The simulation results of the proposed second-order passband ASS (a) adjusting h_2 only. (b) adjusting h_4 only.

And as for the even-mode resonance, an equivalent magnetic wall is inserted at the symmetry plane TT' and the one-port input admittance is derived as:

$$Y_{ine}=j\tau C_1+\frac{j}{\frac{1}{C_{subs}^{\mathrm{n1}}\tau}+\frac{1}{\tau C_2-Y_B}} \tag{38}$$

where

$$\frac{1}{Y_B}=L_{airs}^{\mathrm{n1}}\tau-\frac{C_{subs}^{\mathrm{n2}}+C_4}{C_{subs}^{\mathrm{n2}}\tau C_4+\tau C_3\left(C_{subs}^{\mathrm{n2}}+C_4\right)} \tag{39}$$

Then the angular response of this ASS can be given by:

$$S_{11}=S_{22}=\frac{Y_0^2-Y_{ine}Y_{ino}}{(Y_0+Y_{ine})(Y_0+Y_{ino})} \tag{40}$$

$$S_{21}=S_{12}=\frac{(Y_{ine}-Y_{ino})Y_0}{(Y_0+Y_{ine})(Y_0+Y_{ino})} \tag{41}$$

where $Y_0=1\Omega^{-1}$ is the re-normalized port admittance in the angular domain.

Then, the numerical optimization can be adopted, and the optimized physical dimensions of the second-order ASS with tunable bandwidth are listed in Table. III. For example, when $h_2=4\mathrm{mm}$ and $h_4=10\mathrm{mm}$, the calculated spatial response is derived as:

$$S_{11}=\frac{(-0.06+F(t))}{(-0.06+jE(\tau)+P(\tau))} \tag{42}$$

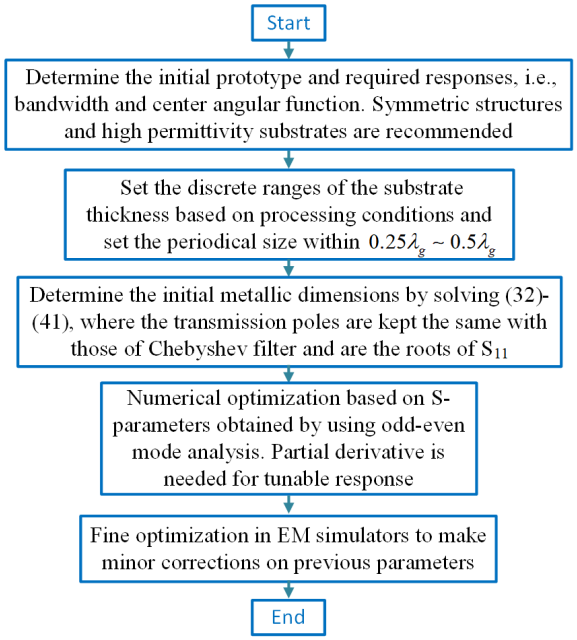

(a)

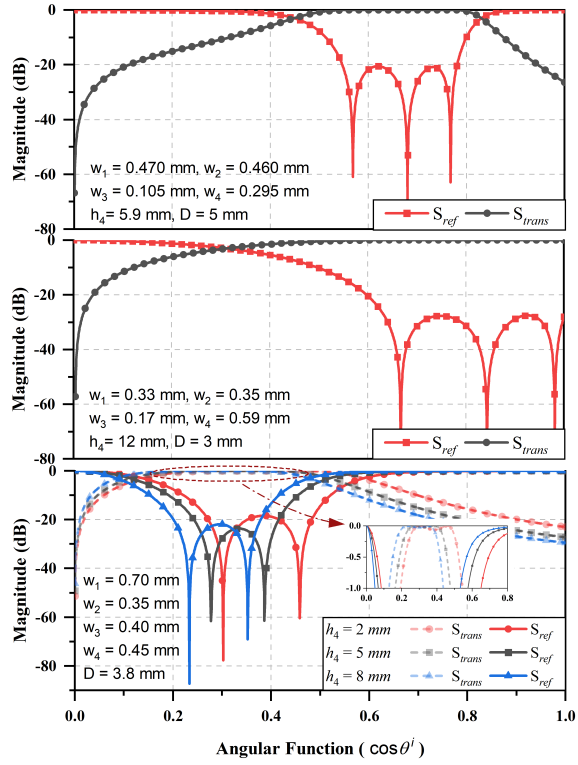

(b)

Fig. 12: Summary of the ASS design. (a) Flowchart of the design procedure. (b) Simulation results of different responses, where two third-order ASS with bandwidth close to the broadside direction and one second-order ASS with tunable center angular function are presented.

where

$$F(\tau)=1.2\tau^2+0.5\tau^4-53.3\tau^6-100\tau^8 \tag{43}$$

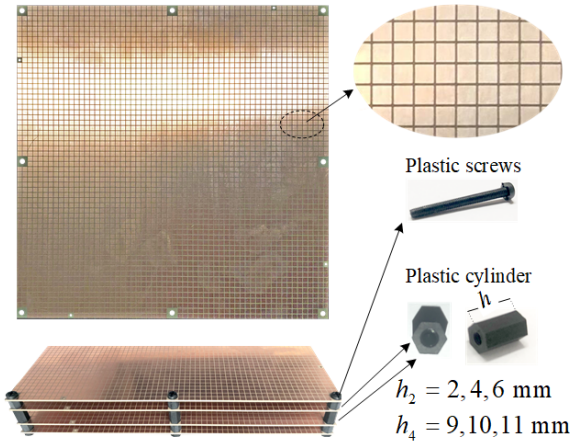

Fig. 13: Photograph of the fabricated prototype

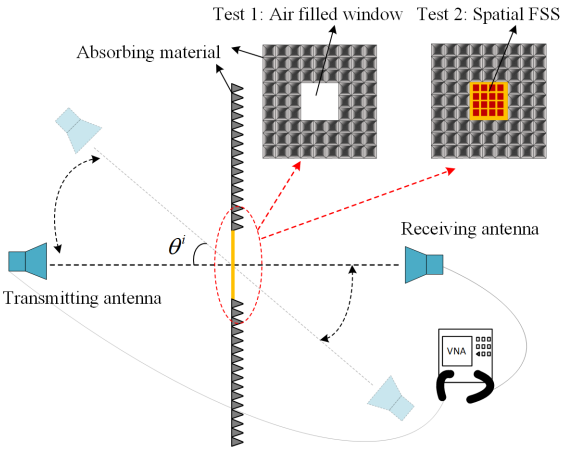

Fig. 14: Setup of the measurement.

$$E(\tau) = 0.1\tau - 4\tau^3 - 6\tau^5 + 16\tau^7 \tag{44}$$

$$P(\tau) = 1.56\tau^2 + 1.2\tau^4 + 52\tau^6 + 100\tau^8 \tag{45}$$

Fig. 11 demonstrated the simulated validation of this design, and the bandwidth tuning of the passband is realized by adjusting the air space lengths. The tunable 3-dB BW of $0.3 \sim 0.5$ in the angular domain is obtained when h_2 and h_4 range from $2mm \sim 6mm$ and $9mm \sim 11mm$, respectively. And in this design, the tunable 20 dB-bandwidth achieved by adjusting the lengths of the air spacers is near $[0.08, 0.22]$ in the angular domain.

Fig. 12(a) shows the general design guidelines for the proposed ASSs. In this design, the genetic algorithm is applied. Machine learning and inverse design methods [24] can also work well since the equivalent circuits proposed are accurate. To further demonstrate this design method, simulation results of different responses are presented in Fig. 12(b). It can be seen that the angular selections are achievable both in the grating direction and the broadside direction. In this work, since only basic patch units and four substrate layers are used, the achievable 20-dB bandwidth is ranged from 0.06 to 0.63 in the angular domain.

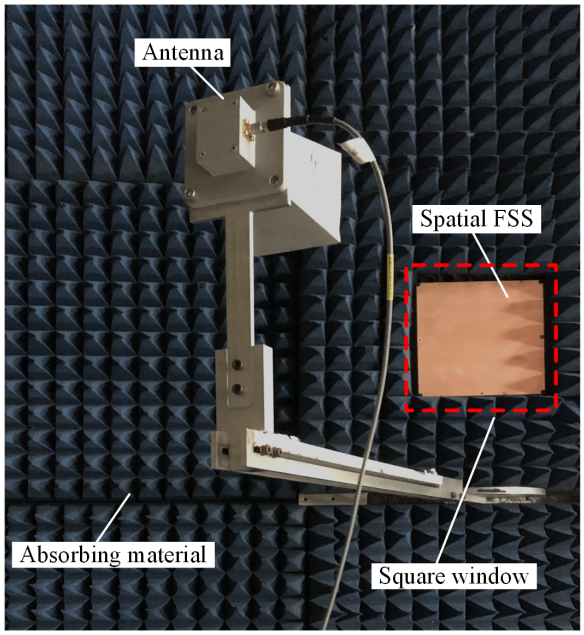

Fig. 15: Photograph of test 2: measuring the transmission coefficient of the fabricated second-order ASS, which is fixed at the air-filled window.

V. Fabrication and Measurement of the Second-Order ASS

As displayed in Fig. 13, the fabricated second-order ASS consists of four identical TP$-1/2$ substrates ($\varepsilon_r = 10.2$, $\tan\delta = 0.0008$). The design consists of 60×60 unit cells, and the overall size is $180\text{mm} \times 180\text{mm}$. Several plastic screws and cylinders are inserted between the substrates to form the air spacers and to fix the position. Bandwidth tuning can be realized simply by adjusting the length of these plastic cylinders.

The prototype is measured with the setup displayed in Fig. 14. The transmitting and receiving antennas are placed on both sides of the absorbing material and are symmetrically tilted away from the normal direction. Crucially, there is a square window of the same size as the fabricated spatial ASS in the center of the absorbing material. And there are two tests required during the measurement: test 1 is to measure the transmission coefficient of the air-filled window S_{21_t1}; test 2 is to measure the transmission coefficient of the fabricated second-order spatial ASS fixed in the window S_{21_t2}. And with the decibel operations, the measured transmission coefficients can be obtained: $S_{trans} = S_{21\_t1} - S_{21\_t2}$ (dB).

The photo of the measurement setup and the measured results are shown in Fig. 15 and Fig. 16, respectively. Due to the limitation of our setup, the measured incidence angle can only vary from $0°$ to $85°$, corresponding to the angular function of $[0.09, 1]$ in the angular domain. Compared with the curves shown in Fig. 11, the measurement results, simulation results and calculation results are in good agreement. As shown in Fig. 17, the performance remains stable in the range from 9 GHz to 11 GHz, and the bandwidth changes from $[0.33, 0.52]$ with the change of the center frequency from $[0.21, 0.36]$ in the angular domain.

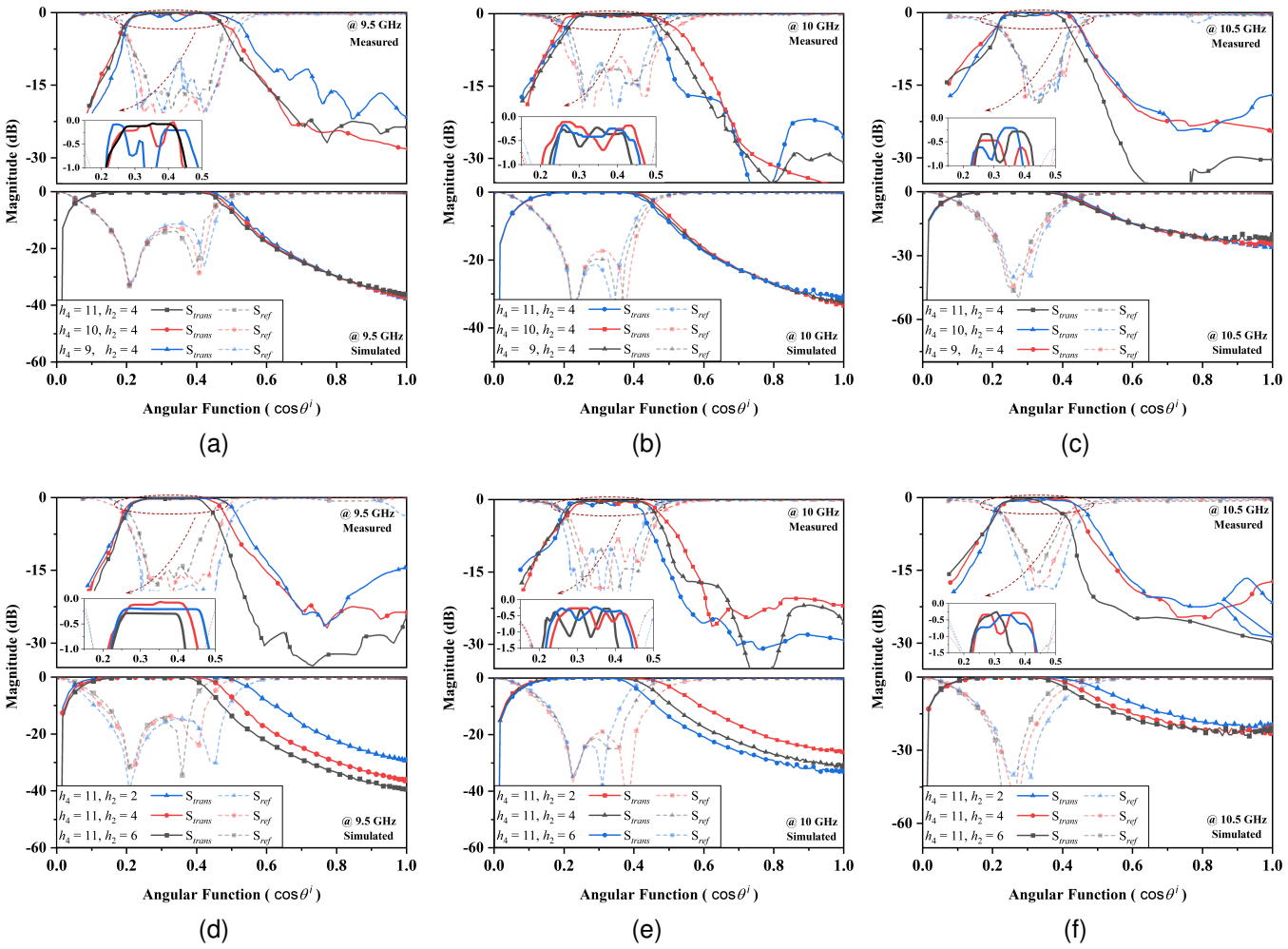

Fig. 16: The measured results of the implemented second-order ASS. The bandpass response (a) versus different h_4 at 9.5 GHz (b) versus different h_4 at 10 GHz (c) versus different h_4 at 10.5 GHz (d) versus different h_2 at 9.5 GHz (e) versus different h_2 at 10 GHz (f) versus different h_2 at 10.5 GHz.

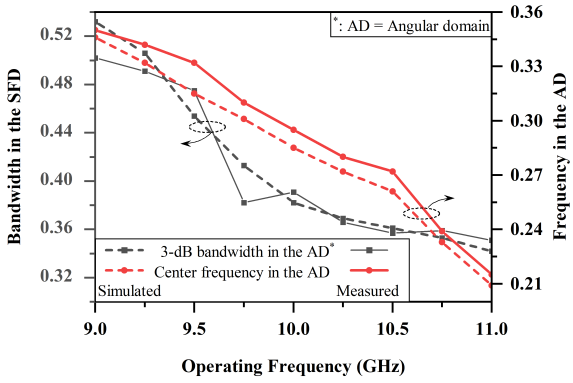

Fig. 17: The measured bandpass response of the implemented second-order ASS versus different operating frequencies.

VI. Discussion

In the angular domain analysis and equivalent circuit mentioned above, the operating frequency is fixed at one point, which emphasises the response to different incidence angles. In this section, the equivalent circuits of these basic units discussed in Section III will be reconstructed to analyze their characteristics in the frequency domain.

Fig. 18 shows the relationship between the S-parameters of the two spatial ASSs proposed in Section V and different operating frequencies. Bandwidths of the passband in the frequency domain are wider when the incidence angle is within the range of 70 to 80 degrees. However, these results are not accidental but can be obtained by equivalent circuit modeling and numerical analysis in the frequency domain.

As shown in Eq. (15), where the operating frequency is not fixed at 10 GHz manually. Once the incidence angle θ, rather than the operating frequency f, is fixed, the equivalent circuit in the frequency domain can be obtained: for the TE incidence wave, the equivalent circuit of the substrate has a series inductor and two parallel capacitors. The same method also applies to TM incidence wave and Eqs. (16), (22) and (24). The equivalent circuits of these basic ASS cells in the frequency domain are summarized in Fig. 19. S-parameters of their combinations can be determined based on circuit analyses

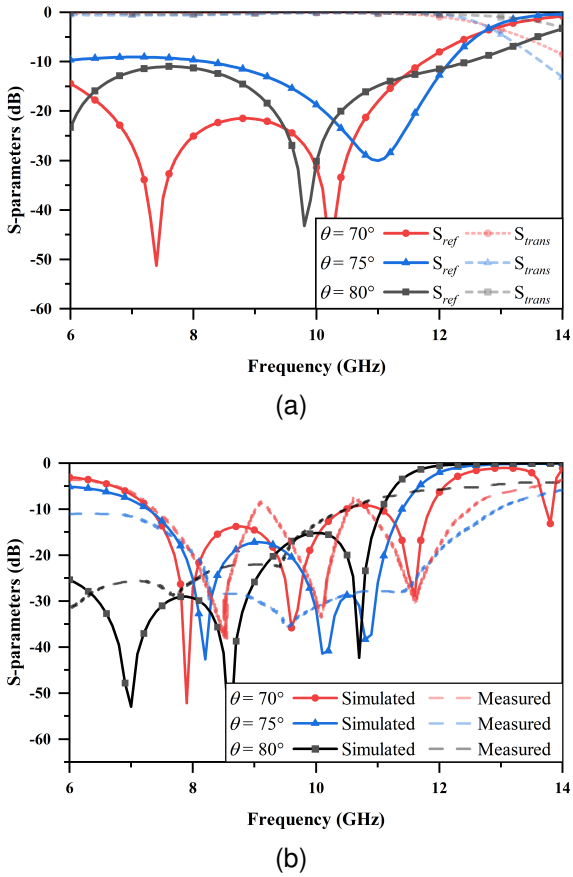

Fig. 18: The response of the two spatial ASSs versus different operating frequencies and different incidence angles. (a) The simulated results of the third-order spatial ASS in Table. II. (b) The simulated results and the measured results of the second-order ASS in Table. III.

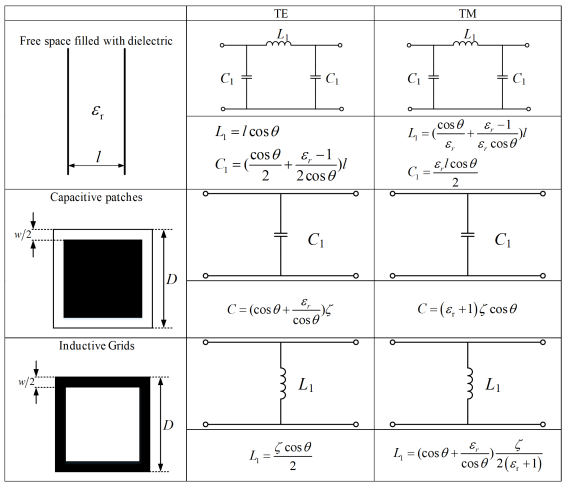

Fig. 19: Summarized equivalent circuits in the frequency domain of the basic ASS cells under different polarization.

and related calculations.

Actually, for a real FSS or ASS, all its response is related to the incidence angle and the operating frequency. To better understand this phenomenon, Fig. 20 shows the transmission coefficient of the proposed second-order ASS versus incidence angle and operating frequency. Specifically, the X-axis represents the incidence angle, the Y-axis represents the operating frequency, and the corresponding color represents the transmission coefficient amplitude. This figure can also be expressed by an analytical formula that contains both the incidence angle and the frequency. It should be realized that such a general analytical formula can be used not only to design the ASS in both the frequency domain and the angular domain, but also to design the transmit-array or the reflect-array once the amplitude and phase of the transmission function are taken into consideration.

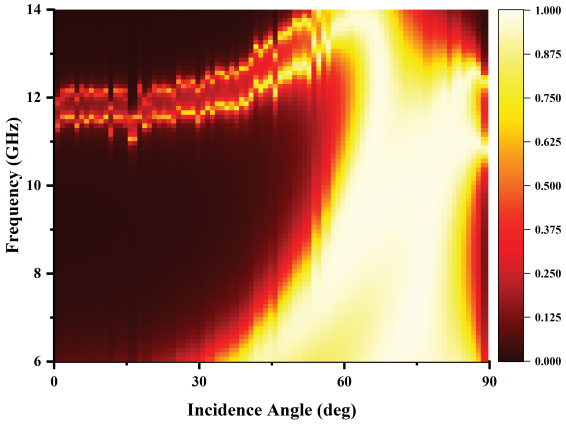

Fig. 20: The transmission coefficient of the proposed second-order ASS versus incidence angle and frequency.

VII. Conclusion

In summary, we have proposed a new efficient synthesis method of frequency selective surfaces in the angular domain based on the accurate equivalent circuit model. The angular dispersion of different components under oblique incidence is simulated by virtual lumped elements in the angular domain. In the whole process of analysis and design, the theoretical calculation is in good agreement with the simulation results. A third-order FSS with bandpass response and a second-order one with a tunable bandwidth are given as design examples. The implemented second-order ASS shows the $[0.33, 0.52]$ tunable bandwidth in the angular domain. The transmission loss is better than 1.2 dB when the incidence angle is 65 to 77 degrees. The simulated results and calculated results are in good agreement with the measured results. The proposed spatial ASS can serve as a potential device in secure communications, radome design, energy harvesting, spatial multiplexing and anti-interference under a specific incidence angle.

Our work is the first step in the study of ASS equivalent circuits. Future work will analyze more complex structures to reduce the spatial ASS profile. Also, by synthesizing the amplitude and phase shift for different incidence angles, a spatial transmit array with high aperture efficiency and low side-lobe level will be designed.

References

[1] B. A. Munk, *Frequency selective surfaces: theory and design*. Wiley, 2000.

[2] B. Munk, *Finite antenna arrays and FSS*. IEEE Press, 2003.

[3] F. Erkmen, T. S. Almoneef, and O. M. Ramahi, "Scalable electromagnetic energy harvesting using frequency-selective surfaces," *IEEE Transactions on Microwave Theory and Techniques*, vol. 66, no. 5, pp. 2433–2441, 2018.

[4] V. Krushna Kanth and S. Raghavan, "Em design and analysis of frequency selective surface based on substrate-integrated waveguide technology for airborne radome application," *IEEE Transactions on Microwave Theory and Techniques*, vol. 67, no. 5, pp. 1727–1739, 2019.

[5] N. Liu, X. Sheng, C. Zhang, and D. Guo, "Design and synthesis of band-pass frequency selective surface with wideband rejection and fast roll-off characteristics for radome applications," *IEEE Transactions on Antennas and Propagation*, vol. 68, no. 4, pp. 2975–2983, 2020.

[6] Z. Zhao, J. Li, H. Shi, X. Chen, and A. Zhang, "A low-profile angle-insensitive bandpass frequency-selective surface based on vias," *IEEE Microwave and Wireless Components Letters*, vol. 28, no. 3, pp. 200–202, 2018.

[7] C. Yepes, D. Cavallo, E. Gandini, S. Monni, A. Neto, and F. E. van Vliet, "Angularly stable frequency selective surface combined with a wide-scan phased array," *IEEE Transactions on Antennas and Propagation*, vol. 66, no. 2, pp. 1046–1051, 2018.

[8] T. Hong, W. Xing, Q. Zhao, Y. Gu, and S. Gong, "Single-layer frequency selective surface with angular stability property," *IEEE Antennas and Wireless Propagation Letters*, vol. 17, no. 4, pp. 547–550, 2018.

[9] W. Yin, H. Zhang, T. Zhong, and X. Min, "Ultra-miniaturized low-profile angularly-stable frequency selective surface design," *IEEE Transactions on Electromagnetic Compatibility*, vol. 61, no. 4, pp. 1234–1238, 2019.

[10] C. Jin, Q. Lv, B. Zhang, J. Liu, S. An, Z. S. He, and Z. Shen, "Ultra-wide-angle bandpass frequency selective surface," *IEEE Transactions on Antennas and Propagation*, vol. 69, no. 9, pp. 5673–5681, 2021.

[11] N. Behdad and M. A. Al-Joumayly, "A generalized synthesis procedure for low-profile, frequency selective surfaces with odd-order bandpass responses," *IEEE Transactions on Antennas and Propagation*, vol. 58, no. 7, pp. 2460–2464, 2010.

[12] X. Yao, M. Bai, and J. Miao, "Equivalent circuit method for analyzing frequency selective surface with ring patch in oblique angles of incidence," *IEEE Antennas and Wireless Propagation Letters*, vol. 10, pp. 820–823, 2011.

[13] Y. Li, L. Li, Y. Zhang, and C. Zhao, "Design and synthesis of multilayer frequency selective surface based on antenna-filter-antenna using minkowski fractal structures," *IEEE Transactions on Antennas and Propagation*, vol. 63, no. 1, pp. 133–141, 2015.

[14] K. Payne, K. Xu, and J. H. Choi, "Generalized synthesized technique for the design of thickness customizable high-order bandpass frequency-selective surface," *IEEE Transactions on Microwave Theory and Techniques*, vol. 66, no. 11, pp. 4783–4793, 2018.

[15] E. Zhu, Z. Wei, X. Xu, and W.-Y. Yin, "Fourier subspace-based deep learning method for inverse design of frequency selective surface," *IEEE Transactions on Antennas and Propagation*, vol. 70, no. 7, pp. 5130–5143, 2022.

[16] R. Mailloux, "Synthesis of spatial filters with chebyshev characteristics," *IEEE Transactions on Antennas and Propagation*, vol. 24, no. 2, pp. 174–181, 1976.

[17] P. Franchi and R. Mailloux, "Theoretical and experimental study of metal grid angular filters for sidelobe suppression," *IEEE Transactions on Antennas and Propagation*, vol. 31, no. 3, pp. 445–450, 1983.

[18] D. Jackson and N. Alexopoulos, "Gain enhancement methods for printed circuit antennas," *IEEE Transactions on Antennas and Propagation*, vol. 33, no. 9, pp. 976–987, 1985.

[19] H. Y. Yang and N. G. Alexopoulos, "Gain enhancement methods for printed circuit antennas through multiple superstrates," *IEEE Transactions on Antennas and Propagation*, vol. 35, pp. 860–863, July 1987.

[20] D. Kinowski, M. Guglielmi, and A. G. Roederer, "Angular bandpass filters: an alternative viewpoint gives improved design flexibility," *IEEE Transactions on Antennas and Propagation*, vol. 43, no. 4, pp. 390–395, 1995.

[21] Young Ju Lee, Sung Hun Jeong, Wee San Park, Jae Seung Yun, and Soon Ick Jeon, "Multilayer spatial angular filter with airgap tuners to suppress grating lobes of 4/spl times/1 array antenna," *Electronics Letters*, vol. 39, no. 1, pp. 15–17, 2003.

[22] J. D. Ortiz, J. D. Baena, V. Losada, F. Medina, and J. L. Araque, "Spatial angular filtering by fsss made of chains of interconnected srrs and csrrs," *IEEE Microwave and Wireless Components Letters*, vol. 23, no. 9, pp. 477–479, 2013.

[23] G. I. Kiani, K. L. Ford, K. P. Esselle, A. R. Weily, and C. J. Panagamuwa, "Oblique incidence performance of a novel frequency selective surface absorber," *IEEE Transactions on Antennas and Propagation*, vol. 55, no. 10, pp. 2931–2934, 2007.

[24] Z. Wei, Z. Zhou, P. Wang, J. Ren, Y. Yin, G. F. Pedersen, and M. Shen, "Equivalent circuit theory-assisted deep learning for accelerated generative design of metasurfaces," *IEEE Transactions on Antennas and Propagation*, vol. 70, no. 7, pp. 5120–5129, 2022.

[25] D. E. Serup, G. F. Pedersen, and S. Zhang, "Dual-band shared aperture reflectarray and patch antenna array for s- and ka-band," *IEEE Transactions on Antennas and Propagation*, pp. 1–1, 2021.

[26] A. Bhattacharyya, *Floquet Modal Functions*. John Wiley & Sons, Ltd, 05 2006, ch. 3, pp. 89–128.

[27] B. Arun, *Frequency Selective Surface, Polarizer, and Reflect Array Analysis*. John Wiley & Sons, Ltd, 05 2005, ch. 9, pp. 295–327.

[28] F. Costa, A. Monorchio, and G. Manara, "An overview of equivalent circuit modeling techniques of frequency selective surfaces and metasurfaces," *The Applied Computational Electromagnetics Society Journal (ACES)*, vol. 29, no. 12, p. 960–976, Aug. 2021.

[29] L. B. Whitbourn and R. C. Compton, "Equivalent-circuit formulas for metal grid reflectors at a dielectric boundary," *Appl. Opt.*, vol. 24, no. 2, pp. 217–220, Jan 1985.

[30] J. S. Hong, *Basic Concepts and Theories of Filters*. John Wiley & Sons, Ltd, 2011, ch. 3, pp. 28–74.

[31] D. M. Pozar, *Microwave engineering; 3rd ed.* Hoboken, NJ: Wiley, 2005.

[32] C. A. Balanis, *Advanced engineering electromagnetics*. Limusa, 1994.

[33] H. Lamb, "On the reflection and transmission of electric waves by a metallic grating," *Proceedings of the London Mathematical Society*, vol. s1-29, no. 1, pp. 523–546, 1897.

[34] I. Palocz and A. A. Oliner, "Equivalent network of a multimode planar grating," *IEEE Transactions on Microwave Theory and Techniques*, vol. 18, no. 5, pp. 244–252, 1970.

[35] S.-W. Lee, G. Zarrillo, and C.-L. Law, "Simple formulas for transmission through periodic metal grids or plates," *IEEE Transactions on Antennas and Propagation*, vol. 30, no. 5, pp. 904–909, 1982.

[36] R. G. Rojas, "Electromagnetic diffraction of an obliquely incident plane wave field by a wedge with impedance faces," *IEEE Transactions on Antennas and Propagation*, vol. 36, no. 7, pp. 956–970, 1988.

[37] S. Tretyakov and C. Simovski, "Dynamic model of artificial reactive impedance surfaces," *Journal of Electromagnetic Waves and Applications - J ELECTROMAGNET WAVE APPLICAT*, vol. 17, pp. 131–145, 01 2003.

[38] G. Goussetis, A. P. Feresidis, and J. C. Vardaxoglou, "Tailoring the amc and ebg characteristics of periodic metallic arrays printed on grounded dielectric substrate," *IEEE Transactions on Antennas and Propagation*, vol. 54, no. 1, pp. 82–89, 2006.

[39] O. Luukkonen, C. Simovski, G. Granet, G. Goussetis, D. Lioubtchenko, A. V. Raisanen, and S. A. Tretyakov, "Simple and accurate analytical model of planar grids and high-impedance surfaces comprising metal strips or patches," *IEEE Transactions on Antennas and Propagation*, vol. 56, no. 6, pp. 1624–1632, 2008.

[40] F. Costa, A. Monorchio, and G. Manara, "Efficient analysis of frequency-selective surfaces by a simple equivalent-circuit model," *IEEE Antennas and Propagation Magazine*, vol. 54, no. 4, pp. 35–48, 2012.

[41] R. C. Compton, L. B. Whitbourn, and R. C. McPhedran, "Strip gratings at a dielectric interface and application of babinet's principle," *Appl. Opt.*, vol. 23, no. 18, pp. 3236–3242, Sep 1984.

[42] S. Tretyakov, *Analytical Modeling in Applied Electromagnetics*, ser. Artech House electromagnetic analysis series. Artech House, 2003.

[43] M. A. Al-Joumayly and N. Behdad, "A generalized method for synthesizing low-profile, band-pass frequency selective surfaces with non-resonant constituting elements," *IEEE Transactions on Antennas and Propagation*, vol. 58, no. 12, pp. 4033–4041, 2010.

[44] R. J. Cameron, C. M. Kudsia, and R. R. Mansour, *Microwave filters for communication systems: fundamentals, design, and applications*. John Wiley & amp; Sons, Inc., 2018.